AGU
ADVANCING EARTH AND SPACE SCIENCE

Geophysical Research Letters

Key Points:
- Gyro-resonance between solar wind ions and right-hand circularly polarized electromagnetic waves results in magnetic field amplification
- Gyro-trapping by the growing magnetic field builds up the plasma density that further enhances the field growth
- The solitary nature of SLAMS stems from the magnetic field envelope where the maximum sets the initial locations for nonlinear growth

Solitary Magnetic Structures at Quasi-Parallel Collisionless Shocks: Formation

Li-Jen Chen[1] ![ORCID], **Shan Wang**[1,2] ![ORCID], **Jonathan Ng**[1,2] ![ORCID], **Naoki Bessho**[1,2] ![ORCID], **Jian-Ming Tang**[3], **Shing F. Fung**[1] ![ORCID], **Guan Le**[1] ![ORCID], **Daniel Gershman**[1] ![ORCID], **Barbara Giles**[1] ![ORCID], **Christopher T. Russell**[4] ![ORCID], **Roy Torbert**[5,6], and **James Burch**[6] ![ORCID]

[1]NASA Goddard Space Flight Center, Greenbelt, MD, USA, [2]Department of Astronomy, University of Maryland, College Park, MD, USA, [3]iDirect Government, Herndon, VA, USA, [4]Department of Earth, Planetary, and Space Sciences, University of California, Los Angeles, CA, USA, [5]Space Science Center, University of New Hampshire, Durham, NH, USA, [6]Southwest Research Institute, San Antonio, TX, USA

Abstract Solitary magnetic structures known as SLAMS (short large-amplitude magnetic structures) have been considered as essential elements of collisionless shocks with quasi-parallel geometries. Yet the physics underlying their formation remains an open question. In this paper, we use measurements from the magnetospheric multiscale mission combined with fully kinetic simulations to study the formation of SLAMS. We find that gyro-resonance between solar wind ions and right-hand circularly polarized electromagnetic waves results in magnetic field amplification. Gyro-trapping by the growing magnetic field builds up the plasma density that further enhances the current and field. The solitary nature of SLAMS stems from a beat-like magnetic field envelope where the maximum sets the initial location for nonlinear growth. Our results present a conceptual advance on SLAMS, and may shed new light on the open question of magnetic field amplification at astrophysical shocks.

Plain Language Summary We integrate MMS measurements and fully kinetic simulations to investigate the nonlinear processes underlying ultra-low-frequency wave growth and evolution into solitary magnetic structures known as SLAMS. The understanding gained here presents a conceptual advance on the formation of SLAMS at planetary bow shocks, and may serve as new insight into how magnetic fields in the interstellar medium are amplified to create an environment for cosmic ray production at astrophysical shocks.

1. Introduction

Solitary magnetic structures known as short large-amplitude magnetic structures (SLAMS) have been envisioned to be the building blocks for quasi-parallel shocks by pioneer studies (e.g., Lucek et al., 2008; Schwartz & Burgess, 1991; Schwartz et al., 1992; Thomsen et al., 1990). Shock observations (e.g., Lucek et al., 2008; Schwartz et al., 1992; references in Eastwood et al. (2005a) and Wilson (2016)) and simulations (Scholer et al., 2003; Tsubouchi & Lembège, 2004) have culminated in a picture that SLAMS develop from electromagnetic waves called the ultra-low-frequency (ULF) waves. In particular, particle-in-cell (PIC) simulations of 1D quasi-parallel shocks with low Mach numbers ($\sim$4) indicate that ULF waves can arise at the foreshock and evolve into SLAMS (Scholer et al., 2003; Tsubouchi & Lembège, 2004). Past work indicates the common occurrence and importance of SLAMS and ULF waves as well as the dynamical connection between them. However, the physics underlying the nonlinear wave development into SLAMS is yet to be understood.

In this paper, we use bow shock measurements and PIC simulations to address the long-standing question of SLAMS formation. The measurements are from NASA's magnetospheric multiscale (MMS) mission. The mission's unprecedented high-resolution measurements enable the plasma response to be investigated and compared with simulation results.

2. Spacecraft Measurements

Two bow shock crossings by MMS will be discussed to provide the ground for simulation and theoretical analysis. The crossings occur when the interplanetary magnetic field (IMF) is dominated by the component along the Sun-Earth line. The reported magnetic fields (128 samples/s) are from the Flux Gate
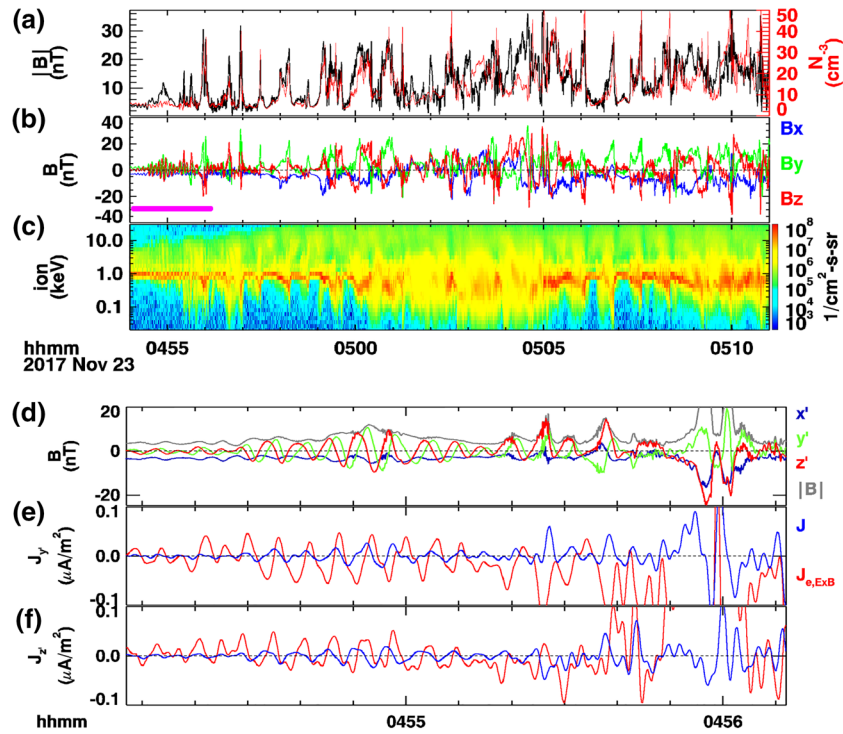
Figure 1. An overview of example solitary magnetic structures (SLAMS) and growing ULF waves observed by MMS1. (a) The magnetic field amplitude |B| and plasma density N. (b) The magnetic field vector in GSE. (c) Energy flux (1/cm³-s-sr) of ions from 10 eV to 30 keV. The magnetic field and current densities in the interval marked by the magenta bar in (b) are shown in (d)–(f) in field-aligned coordinates (where x' is antiparallel to B_0; y' and z' are perpendicular to B_0) that are equivalent to the xyz coordinates in PIC (Section 3). The y' and z' components of J (calculated from the curlometer technique (Robert et al., 1998) using the magnetic fields measured by all four spacecraft) and $J_{e,ExB}$ are plotted in the plasma frame.

Magnetometer (Russell et al., 2014), electric fields (32 samples/s) from the double probes in the FIELDS suites (Ergun et al., 2014; Lindqvist et al., 2014; Torbert et al., 2014), and electron (30 ms/sample) as well as ion (150 ms/sample) data from the Fast Plasma Investigation (Pollock et al., 2016).

2.1. SLAMS Formation Under Anti-Sunward IMF

Intense magnetic fluctuations (Figures 1a and 1b) are generated at the terrestrial bow shock, as the IMF turns quasi-parallel to the shock normal before 5 UT on November 23, 2017. The plasma density in the upstream solar wind is 4.1 cc (average from OMNI 0454 to 0510 UT). The averaged IMF from OMNI is used as the upstream magnetic field $B_0 = 2.7$ (−0.942, 0.327, 0.075) nT, about 20° from $−x_{GSE}$. The Alfvèn Mach number $M_A \sim 12$, ion beta ~ 1, electron beta ~ 3, and the magnetosonic Mach number ~ 6. The angle between B_0 and the shock normal is 35° (based on a shock model (Farris et al., 1991)). The location of MMS is GSE [13.2, 7.2, 2.6]R_E at 5 UT, approximately 0.1R_E from the bow shock MMS exited at ~0450 UT (not shown).

The solitary magnetic structures with both highly enhanced magnetic field strengths (|B|) and plasma densities (N) shown in Figure 1a are the primary subject of investigation. These structures are consistent with those known in the literature as SLAMS (e.g., Schwartz & Burgess, 1991). The purpose of calling them solitary structures will become clear by the end of the simulation section. We will use the two terms interchangeably in this paper.

Examples of SLAMS and their preceding low-frequency electromagnetic waves (ULF waves) presented in Figure 1 suggest that SLAMS and ULF waves are dynamically connected, as envisioned by past observation

(e.g., Lucek et al., 2008; Schwartz et al., 1992) and simulation studies (Scholer et al., 2003; Tsubouchi & Lembège, 2004). The waves (and those in Section 2.2) belong to the 3 s ULF category that is right-hand circularly polarized with respect to B_0 and propagates earthward in the spacecraft frame (Hobara et al., 2007; Le et al., 1992) (to be further discussed later). The three components of the magnetic field show growing quasi-sinusoidal waves in the beginning of the interval, followed by a series of SLAMS with intense B_y and B_z exhibiting a time scale similar to that of the ULF wave. The $|B|$ and N variations are positively correlated for both ULF waves and isolated SLAMS. Most SLAMS in the shown interval contain a sharp bipolar B_z, which are likely to be further compressed into thin current sheets that are conducive to magnetic reconnection (Bessho et al., 2019, 2020; Gingell et al., 2019, 2020; Wang et al., 2019, 2020a).

For every SLAMS, correlated with the amplified $|B|$ and N is the energy-flux enhancement of ions with energies both below and above the solar wind energy ($\sim$1 keV), extending from approximately a hundred eV or below to above 10 keV (Figure 1c). The SLAMS sandwiched by the solar wind population at 1 keV are solitary magnetic structures.

The SLAMS and ULF wave in Figure 1 propagate antisunward in the spacecraft frame, based on timing analysis of the magnetic fields measured by the four spacecraft. The propagation directions of the SLAMS observed during 04:56–05:11 UT are 4–37° from $-x_{GSE}$, and the speeds range from 137 to 219 km/s in the spacecraft (cruising away from the Earth with a speed of a few km/s) frame, corresponding to 5–8V_A ($V_A = 33$ km/s $V_{sw} \sim 420$ km/s is the Alfvèn speed) going upstream in the background solar wind (SW) frame ($V_{sw} \sim 420$ km/s along $-x_{GSE}$), approximately in the reported range of 1–6V_A for smaller amplitude SLAMS (e.g., Mann et al., 1994). The scale size along x (or along propagation) is $\sim$1,000–3,000 km $\sim$ 10–30d_i, consistent with previous SLAMS observations (e.g., Lucek et al., 2008). The ULF wave at 045440–045510 UT propagates with a phase velocity (V_{ph}) of 340[−0.91, 0.36, 0.21] km/s in GSE, approximately 12° from the background magnetic field (taken from 04:54 UT), and 25° from $-x_{GSE}$. Transforming the spacecraft frame V_{ph} to the plasma frame (defined by the bulk velocity of all ions at 04:54 UT) which lies between the solar wind and the spacecraft frames due to the inclusion of ions streaming back (backstreaming) toward the Sun, the phase velocity is 10 km/s (0.3V_A) earthward and the polarization is right handed.

The peak $|B|$ in the large-amplitude ULF reaches 12 nT and steepened ULF 16 nT (Figures 1a, 1b, and 2a). Both exceed the defining criterion of SLAMS ($|B|/B_0 > 2$, (Schwartz et al., 1992)). However, we will refer to them as large-amplitude and steepened ULF waves, as they are intermediate stages to the solitary magnetic structures (the isolated structure with intense $|B|$ and N enhancement at 0456 UT and thereafter).

The observed ULF wave is circularly polarized with the wave B_y lagging behind B_z by about 90° (Figures 1d and 2b), described by $B_y \sim iB_z$ and as right-hand polarized in the spacecraft frame. The ULF wave satisfies the gyro-resonant condition with the solar wind ions (Gary, 1991) with a resonant velocity of 400–520 km/s (based on $\omega - k \cdot V_{res} = -\omega_{ci}$), within one V_{th} (30 km/s based on OMNI T_i of 5 eV) from the solar wind ion bulk velocity along k (382 km/s). In-depth analysis of the ULF waves and their interaction with ions is reported in a separate publication (Wang et al., 2020b).

To gain insight into the ion dynamics during growing ULF waves and SLAMS, the ion velocity distribution function (summed over v_y and v_z) in the v_x space is presented in time series (Figure 2d). Note that the convection along x enables the translation from time to x. As such, Figure 2d can be viewed as x–v_x phase space and changes in the convection velocity (e.g., the ULF wave has a larger x velocity toward the Earth than SLAMS) stretch or compress the spatial variations in x.

The growing B_{yz} being transverse to the background magnetic field gyro-turns the particles, resulting in one to multiple gyro-reflections (these we term gyro-trapping) within the enhanced $|B|$ region and leading to density buildup. One example is marked at the steepened ULF wave (gray dotted line at $\sim$045526 UT) in Figure 2. The amplitude of B_{yz} increases by approximately a factor of four from the minimum to maximum, and the density by a factor of 2. Gyro-trapping enhances the density, which in turn contributes to enhancements of the current and field. This picture is supported by tracing all particles (not shown) at density (and $|B|$) peaks during SLAMS formation in our PIC simulation.

The backstreaming ion phase space density (PSD) increases as the large-amplitude ULF wave continues to be amplified (Figures 2d–2f). As illustrated by example v_x–v_z distributions (Figure 2g), the addition of a cold
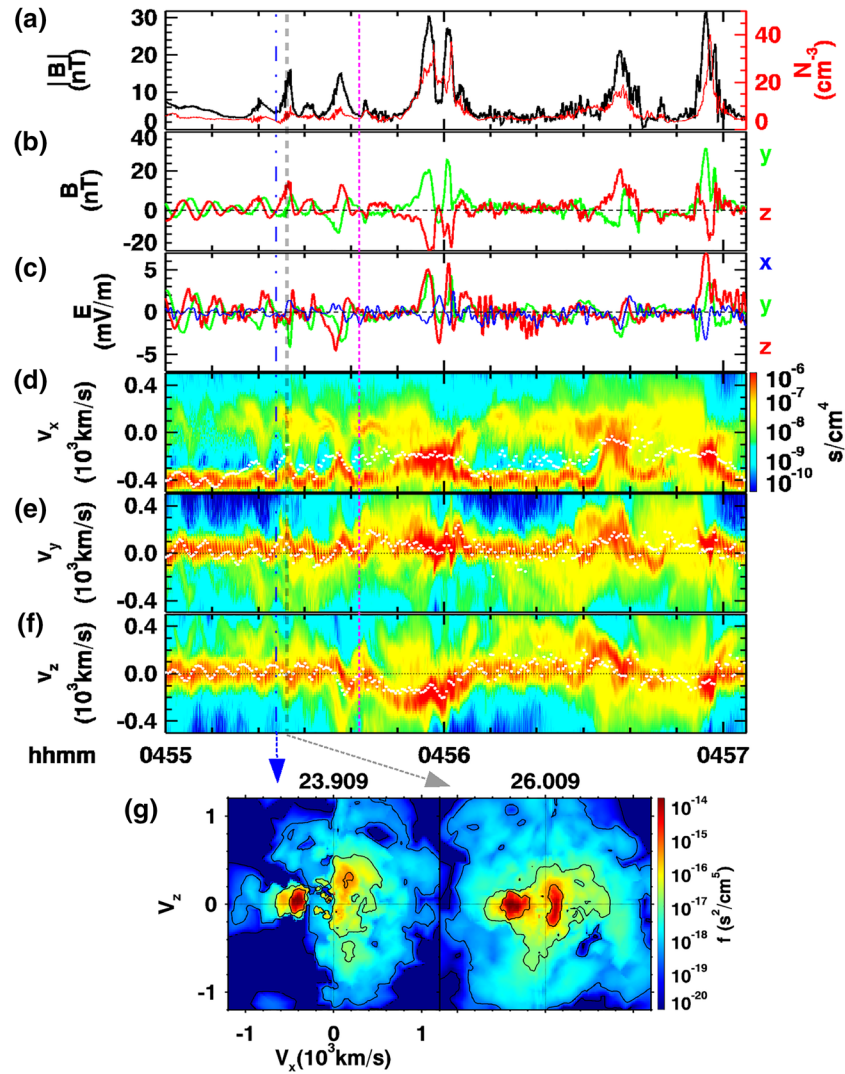
Figure 2. Zoom in view of the first few SLAMS and the preceding ULF waves. (a) The magnetic field amplitude $|B|$ and plasma density N. (b) Magnetic field components B_y and B_z. (c) Electric field components E_{xyz}. (d)–(f) Time series of the reduced ion velocity distributions in v_x, v_y, and v_z. Electron bulk velocities are overplotted as white dots. (g) Ion distribution functions in v_x–v_z showing the evolution of the solar wind and backstreaming ions. All vectors are in GSE. The magenta vertical dashed line indicates the time where the plasma conditions are taken to guide our simulation parameters, while the gray line marks an example where the solar wind V_x is largely gyro-turned to V_y.

and dense population (likely due to solar wind ions reflected off a growing structure that passed by MMS) boosts the backstreaming ion PSD at the steepened ULF. Moreover, the overall ion distribution becomes hotter and more diffuse, as solar wind and backstreaming ions undergo multiple gyration and mix. Right at the transition from growing ULF to the first solitary structure is a brief moment (marked by a magenta vertical line) when the backstreaming ion PSD is more intense than before and the solar wind ions are approximately at their upstream state: $V_x \sim -420$ km/s, $V_y \sim V_z \sim 0$, while the electron flow V_{ex} (white dots) is ~ -200 km/s (approximately the ion bulk flow, not shown). For the marked time, $n_b/N = 0.4$, $V_b - V_{sw}$ is $14V_A$ along $-B_0$ (approximating B_0 to be along $-x_{GSE}$), where n_b and V_b are the density and bulk velocity of backstreaming ions. In the plasma frame, V_b along $-B_0$ is $8.4V_A$. The SW ion $\beta \sim 1$, $T_b/T_{sw} = 100$, $T_e/T_{sw} = 3.6$. This state of the plasma inspires the parameters for our PIC simulations (Section 3).
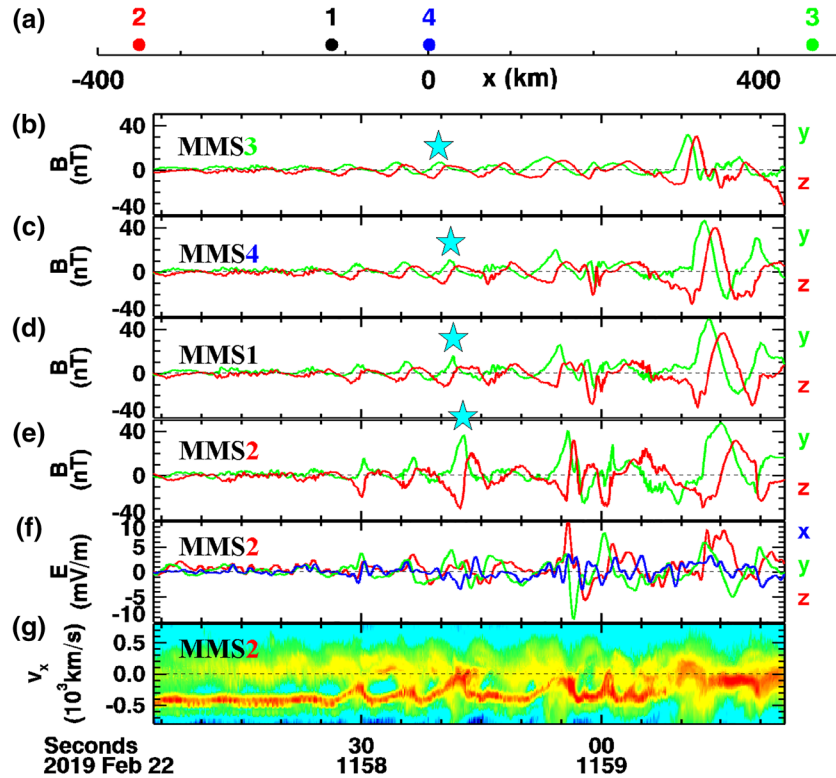
Figure 3. Evolution of the ULF wave into SLAMS observed with a colinear MMS spacecraft configuration. The spacecraft separation along x_{GSE} is illustrated in (a). The magnetic field components B_y and B_z from MMS 3 (b), 4 (c), 1 (d), and 2 (e), in the order of distance from earth farthest to nearest. (f) Electric field components from MMS 2. (g) The reduced ion velocity distribution (colorbar in Figure 2d) in v_x. The stars call out an example growing B_y peak as it travels by the four spacecraft.

2.2. SLAMS Formation Under Sunward IMF

In this section, growing ULF waves evolving into SLAMS are captured by the four co-linearly configured MMS spacecraft separated by hundreds of kilometers, sufficient to track the evolution of the structure. The ULF steepening into SLAMS discussed in the previous section is registered by MMS in a tetrahedron formation with a spacecraft separation of 22 km on average, not allowing monitoring of the structure evolution. For the colinear case, $M_A \sim 10.5$ and the position of MMS 3 is GSE $[14.2, 0.2, 1.5]R_E$ at 1159 UT on February 22, 2019. The IMF is 4.1$[0.9, 0.4, -0.2]$ nT, $\sim 26°$ from $+x_{GSE}$.

The observed magnetic fields are approximately circularly polarized with B_y leading B_z by $\sim 90°$ (Figure 3), described by $B_y \sim -iB_z$ and as right-hand polarized in the spacecraft frame (IMF dominated by $B_x > 0$). Magnetic field components registered by the four spacecraft indicate growing ULF waves and eventually evolving into SLAMS at the MMS3 location as well as further downstream observed by the other three spacecraft hundreds of kilometers apart along the propagation direction (Figure 3a). The upstream magnetic field (4.1 nT) has been amplified by more than a factor of 10 (Figures 3c–3e). The ion reduced distribution function in v_x indicates intensification of the backstreaming ion PSD as well as V_x decrease and heating of the solar wind ions at SLAMS (Figure 3g), similar to the features in Figure 2d.

The structure speed in the spacecraft frame decreases as the magnetic field grows, consistent with the trend of decreasing speeds from ULF waves to SLAMS observed in the first event, previous studies, and our PIC simulations. The propagation directions determined by the Minimum Variance Analysis (MVA) of magnetic fields measured by MMS 3, 4, 1, and 2 are $k_3 = [-0.694, -0.715, -0.085]$, $k_4 = [-0.841, -0.521, -0.146]$, $k_1 = [-0.884, -0.449, -0.128]$, and $k_2 = [-0.945, -0.272, -0.182]$ in GSE. These angles indicate that the propagation is more aligned with x_{GSE} as the structure propagates toward the Earth and as it grows. The prop-

agation speeds are 374 (MMS3-4), 360 (MMS4-1), and 207 (MMS1-2) km/s, based on the spacecraft separations (spacecraft pairs indicated in the parentheses following the respective speeds) along x_{GSE} and the corresponding time delays from the magnetic field correlation analyses for the interval 11:58:38–11:58:45 UT. The bulk V_i along x_{GSE} is 353 km/s, smaller than the V_{ph} determined by MMS3-4 and MMS4-1, indicating that the wave propagates earthward and the polarization is right handed in the plasma frame. The gyro-resonant velocity is 427–513 km/s (based on analysis of MMS3 magnetic fields from 11:58:23–34 UT), within one thermal speed (31 km/s) from the solar wind velocity along k (406 km/s).

To summarize the observations, both MMS events show isolated SLAMS developed from ULF waves that are (1) right-hand polarized and propagate earthward in the plasma frame and (2) gyro-resonant with a significant subset of the solar wind ions. The presented SLAMS properties (characteristic time scales and waveforms) differ from the structures known as shocklets (e.g., Le & Russell, 1994) which are in part associated with 30 s ULF waves (e.g., Hoppe & Russell, 1983) that gyro-resonate with backstreaming ions (Eastwood et al., 2005b).

3. Particle-in-Cell Simulations

This section presents results from a proof-of-concept simulation to demonstrate that isolated SLAMS develop from an initial condition informed by the MMS observation discussed in Section 2.1: two counterstreaming ion populations with equal drift speeds with respect to the electrons; the SW population at $V_{sw} = -10V_A$; the backstreaming population at $V_b = 10V_A$; the temperature ratio $T_b / T_{sw} = 100$; $T_e / T_{sw} = 2$; $n_b / n_{sw} = 1$; a uniform background $B_0 = (-0.067,0,0) m_e c / |e| d_e$, where m_e is the electron mass, c is the speed of light, e is the electron charge, and d_e is the electron inertia length. Other parameters are: the mass ratio $m_i / m_e = 100$, electron plasma to cyclotron frequency ratio $\omega_{pe} / \omega_{ce} = 15$, and SW ion beta $\beta_{sw} = 1$. The n_b / n_{sw} used here is higher than that in prior studies (e.g., Gary, 1991) and can be reduced by increasing V_b while keeping $n_b V_b / [(n_b + n_{sw})\beta_{sw} V_A]$ (the backstreaming ion current in the plasma frame) the same or slightly lower for SLAMS with enhanced N to form. The simulation, conducted using the VPIC code which solves a system of relativistic Vlasov-Maxwell equations (Bowers et al., 2008), has one spatial and three velocity dimensions.

Solitary structures with amplified $|B|$ and N (Figure 4a) are developed from the initial electromagnetic waves. These waves are polarized as $B_y \sim iB_z$ (B_y lagging behind B_z by ~90°, Figures 4e–4f), and classified as right-hand polarized in the plasma frame. Bipolar and tripolar pulses (Figure 4b) resemble those observed by MMS (Figures 2 and 3). Electric field components both transverse (E_{yz}) and longitudinal (E_x) to the propagation are generated (Figure 4c), consistent with those observed by MMS (Figures 2c and 3f). A negative E_x pulse associated with an SLAMS developed from ULF waves has been produced in a shock simulation ($M_A = 4$) (Tsubouchi & Lembège, 2004). Negative E_x plays a role in reflecting the backstreaming ions toward $-x$, and hence increasing the ion thermal spread, as seen in our PIC simulations (Figure 4d) and MMS observations (e.g., the SLAMS at ~0457 UT in Figures 2c–2d).

The waveforms of B_{yz} from earlier times exhibit a beat-like envelope feature (Figures 4e–4f) similar to that observed by MMS (Figure 1d). The $|B|$ peaks of the envelopes set preferred locations for wave growth. Hence, the magnetic field amplification is not uniform for the initial waves, but focuses on isolated spots. The density enhancement and negative E_x start to develop at the maximum of the wave envelope as the $B_y \sim iB_z$ mode grows (Figure 4g). The exact cause of the envelope requires investigations beyond the scope of this paper. We note that the ratio between the sound speed and the Alfvèn speed exceeds one for most of the MMS interval (Figure 1d), within the regime unstable to the beat-mode parametric instability (Hollweg, 1994).

The dominant wave mode leading to the solitary magnetic structure is in gyro-resonance with the solar wind ions in our simulation. This mode is known in the literature as the nonresonant mode because it does not gyro-resonate with the backstreaming ions (e.g., Gary, 1991; Weidl et al., 2019a, 2019b). Before the formation of solitary structures at $t\omega_{ci} \sim 14$, the wave propagates at $V_{ph} = -5V_A$ with a wave number of $kd_i \sim -0.18$. The cyclotron resonant velocity is $V_{res} = V_{ph} + \omega_{ci} / k = -10.6V_A$, within one SW ion thermal speed ($1V_A$) from the SW ion bulk velocity of $-10V_A$, satisfying the gyro-resonant condition (Gary, 1991). The gyro-resonance with SW ions and wave properties is consistent with results from a linear dispersion
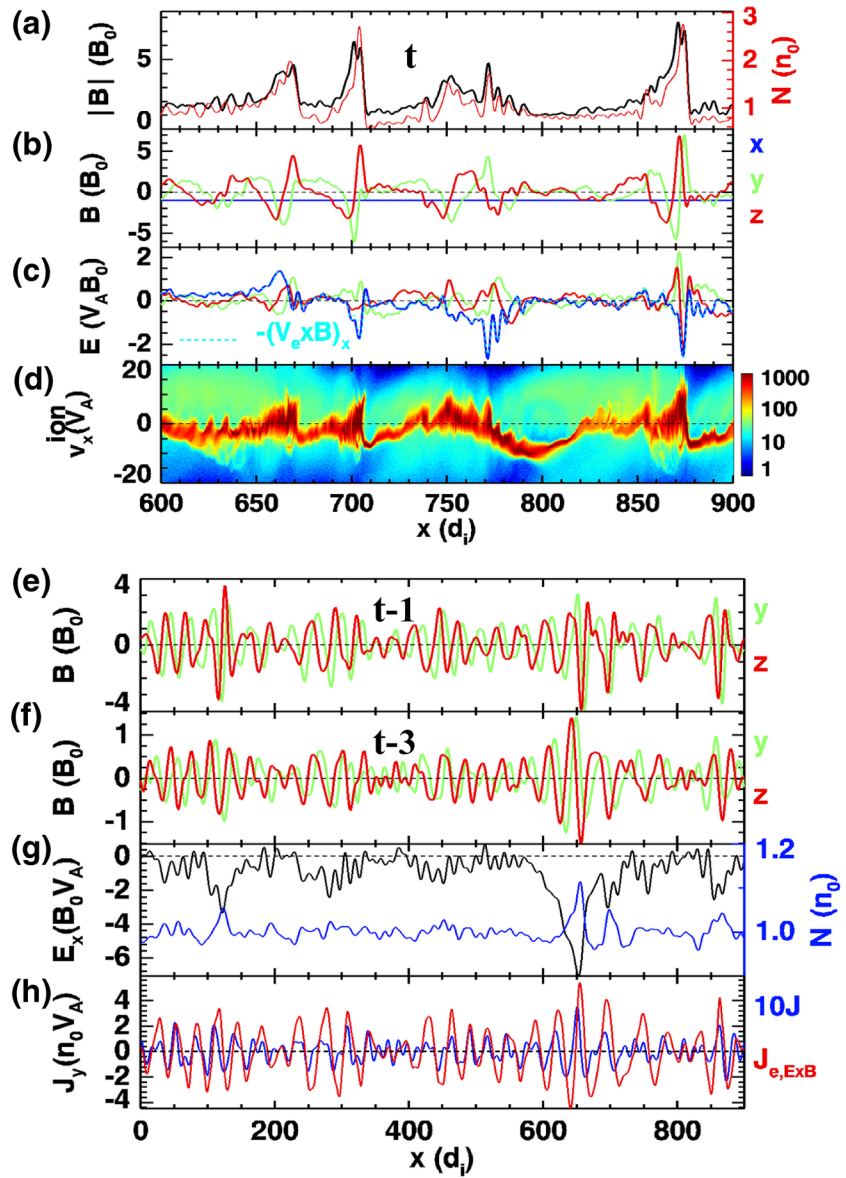
Figure 4. Examples of solitary magnetic structures from a PIC simulation. (a) The magnetic field amplitude and plasma density (N). (b) Magnetic field components B_{xyz}. (c) Electric field E_{xyz} and the x component of $-V_e \times B$. (d) The ion phase space x–v_x. Data in (a)–(d) are taken from $t\omega_{ci} = 16.5$ (labeled as t in a). (e)–(f) show $B_{y,z}$ at $t\omega_{ci} = 15.5$ and 13.5, respectively. (g) E_x and N showing the maxima of the wave envelopes set isolated locations for field and density amplification. (h) The y components of J and $J_{e,ExB}$. (f)–(h) are from $t-3$.

solver which predicts the maximum growth rate at $-x$ propagation, right-hand polarization, $kd_i \sim -0.19$, and $V_{res} = V_{ph} + \omega_{ci} / k = -10.1V_A$.

The ion phase space x–v_x (Figure 4d) shows that at SLAMS, the SW ions are heated and their bulk V_x has been reduced to approximately the electron bulk flow ($V_{ex} \sim 0$), just as observed by MMS (Figure 2d where the $V_{ex} \sim -200$ km/s in the spacecraft frame). The upstream edge of the SLAMS (e.g., at $x/d_i \sim 705$ in Figure 4d) marks the most probable gyro-reflection point of the SW ions, according to particle tracing using PIC fields. The backstreaming ion thermal speed is the same as V_b initially in our simulation. The more isotropic, hot, and diffuse ion population develops at the downstream (left) edge of SLAMS (Figure 4d) as a product of backstreaming ions reflecting off SLAMS, different from the process discussed in prior work

that suggested diffuse ions as a precondition for SLAMS formation (Dubouloz & Scholer, 1993; Giacalone et al., 1993).

4. Wave Growth and Polarization

MMS observations and PIC simulations discussed in the previous sections indicate that the right-hand circularly polarized electromagnetic wave propagating in the the solar-wind direction in the plasma frame grows to large amplitudes and develops into solitary magnetic structures. In this section, we point out the connection between the observed wave growth and polarization based on an approximate relationship between the current density J perpendicular to B_0 and the electron $E \times B$ drift current density $J_{e,ExB} \equiv eN E \times B / |B|^2$. Electrons are magnetized and follow the $E \times B$ drift. If ions are also magnetized, the net $E \times B$ drift current would be zero. The unmagnetized ion dynamics leads to a finite $E \times B$ drift current as well as a current perpendicular to $E \times B$. MMS measurements show that the transverse component of J leads $J_{e,ExB}$ by a small phase shift for the quasi-sinusoidal part of the ULF wave interval (up to $\sim$045512 UT in Figures 1d–1f). Similar phase relationships are observed in the second MMS event (not shown) and PIC simulations (Figure 4h).

Consider the setup in Section 3, the fields can be written as $E(t) = \left[0, \tilde{E}_y(t)e^{ikx}, \tilde{E}_z(t)e^{ikx} \right]$ and $B(t) = \left[B_0, \tilde{B}_y(t)e^{ikx}, \tilde{B}_z(t)e^{ikx} \right]$. The wave fields and the current density are related through the Maxwell equations: $\partial_t \tilde{B}_{y(z)}(t) = \pm ik\tilde{E}_{z(y)}(t)$ (the minus sign is for the component in the parentheses) and $\mu_0 \tilde{J}_{y(z)} = \mp ik\tilde{B}_{z(y)}$. The phase of $\tilde{J}$ is ahead of $\tilde{J}_{e,ExB}$ by less than $\pi/2$, enabling us to write $\alpha \tilde{J}_{y(z)} = \tilde{J}_{e,E\times B,y(z)}$, where $\alpha = \alpha_R + i\alpha_I$ is a complex number with both $\alpha_R > 0$ and $\alpha_I > 0$. Combining $\alpha \tilde{J}_{y(z)} = \tilde{J}_{e,E\times B,y(z)} \approx \pm \frac{eN}{B_0} \tilde{E}_{z(y)}$ with the two Maxwell equations, we obtain a set of differential equations, $\frac{\partial}{\partial t} \tilde{B}_{y(z)}(t) = \pm ik\tilde{E}_{z(y)}(t) = i\frac{\alpha k B_0}{eN} \tilde{J}_{y(z)} = \pm \frac{\alpha k^2 B_0}{eN\mu_0} \tilde{B}_{z(y)}$. The equations can be arranged into the following form for the two polarizations: $\frac{\partial}{\partial t} \tilde{B}_{\pm}(t) = \mp i\frac{\alpha k^2 B_0}{eN\mu_0} \tilde{B}_{\pm}$ where $\tilde{B}_{\pm}(t) = \tilde{B}_y \pm i\tilde{B}_z$. The growth solution is $\tilde{B}_+ \sim e^{-i\omega t + \gamma t}$, where $\omega = \frac{\alpha_R k^2 B_0}{eN\mu_0} > 0$ and $\gamma = \frac{\alpha_I k^2 B_0}{eN\mu_0} > 0$ for $B_0 < 0$ (note: $e < 0$). For $B_0 > 0$, the growth solution is $\tilde{B}_-(t) = \tilde{B}_y - i\tilde{B}_z$.

The above discussion connects the observed J-$J_{e,ExB}$ phase relationship with the polarization of the growing wave. For the first MMS event and the PIC simulation with a background magnetic field $B_0 < 0$, the ULF wave exhibits a $B_y \sim iB_z$ polarization, corresponding to the $\tilde{B}_+$ solution, while for the second event, $B_0 > 0$, and the growing wave has a polarization $B_y \sim -iB_z$, corresponding to the $\tilde{B}_-$ solution.

5. Summary, Discussion, and Conclusion

In summary, we integrate MMS measurements and PIC simulations to investigate the formation of solitary magnetic structures known as SLAMS in the shock literature, and achieve the following new understanding: (1) Gyro-resonance between solar wind ions and right-hand circularly polarized electromagnetic waves results in magnetic field amplification, (2) gyro-trapping by the growing magnetic field builds up the plasma density that further enhances the magnetic field growth, (3) high amplification of the magnetic field occurs at discrete (isolated) locations at the $|B|$ maximum of the wave envelope where the initial density enhancement and longitudinal electric field develop. Our work points out new directions for future research, for example, the origin of the beat-like wave envelope and the plasma dynamics associated with the longitudinal electric fields.

The nonresonant mode found to dominate the magnetic field amplification in our study corresponds to the Bell instability in astrophysics (e.g., Bell, 2004; Weidl et al., 2019a; Zweibel & Everett, 2010). A long-standing open question concerns whether the primary instability mediating the magnetic field amplification resonates or does not resonate (Bell instability) with the backstreaming ions at supernova remnant (SNR) shocks. Our results show that the dominant mode gyro-resonates with the solar wind ions, presenting a

case for the background-gyro-resonant character of the Bell instability (Weidl et al., 2019a), and may bear implications to the SNR shocks as the essential physics of magnetic field amplification is established to be qualitatively the same for shocks with the Alfvèn Mach number 5–500 (Caprioli & Spitkovsky, 2013, 2014a, 2014b).

In conclusion, our work addresses the nonlinear processes underlying ULF wave growth and evolution into isolated SLAMS. The understanding gained here presents a conceptual advance on the formation of SLAMS at planetary bow shocks, and may serve as new insight into how magnetic fields in the interstellar medium are amplified to create an environment for cosmic ray production at astrophysical shocks.

Data Availability Statement

MMS data are available at MMS Science Data Center (https://lasp.colorado.edu/mms/sdc/), and simulation at https://zenodo.org/record/4257050. Computation resources supporting this work were provided by NASA HECC and NSF Frontera.

References

Bell, A. R. (2004). Turbulent amplification of magnetic field and diffusive shock acceleration of cosmic rays. *Monthly Notices of the Royal Astronomical Society*, *353*, 550–558. https://doi.org/10.1111/j.1365-2966.2004.08097.x

Bessho, N., Chen, L.-J., Wang, S., Hesse, M., & Wilson, L. B., III (2019). Magnetic reconnection in a quasi-parallel shock: Two-dimensional local particle-in-cell simulation. *Geophysical Research Letters*, *46*, 9352–9361. https://doi.org/10.1029/2019GL083397

Bessho, N., Chen, L.-J., Wang, S., Hesse, H., Wilson, L. B., III, & Ng, J. (2020). Magnetic reconnection and kinetic waves generated in the Earth's quasi-parallel bow shock. *Physics of Plasmas*, *27*(9), 092901. https://doi.org/10.1063/5.0012443

Bowers, K. J., Albright B. J., Yin L., Bergen B., & Kwan T. J. T. (2008). Ultrahigh performance three-dimensional electromagnetic relativistic kinetic plasma simulation. *Physics of Plasmas*, *15*(5), 055703. https://doi.org/10.1063/1.2840133

Caprioli, D., & Spitkovsky, A. (2014a). Simulations of ion acceleration at non-relativistic shocks. I. Acceleration efficiency. *The Astrophysical Journal*, *783*, 91. https://doi.org/10.1088/0004-637X/783/2/91

Caprioli, D., & Spitkovsky, A. (2014b). Simulations of ion acceleration at non-relativistic shocks. II. Magnetic field amplification. *The Astrophysical Journal*, *794*, 46. https://doi.org/10.1088/0004-637X/794/1/46

Caprioli, D., & Spitkovsky, A. (2013). Cosmic-ray-induced filamentation instability in collisionless shocks. *The Astrophysical Journal Letters*, *765*, L20. https://doi.org/10.1088/2041-8205/765/1/L20

Dubouloz, N., & Scholer, M. (1993). On the origin of short large amplitude magnetic structures upstream of quasi-parallel collisionless shocks. *Geophysical Research Letters*, *20*, 547. https://doi.org/10.1029/93GL00803

Eastwood, J. P., Balogh, A., Lucek, E. A., Mazelle, C., & Dandouras, I. (2005a). Quasi-monochromatic ULF foreshock waves as observed by the four-spacecraft cluster mission: 1. Statistical properties. *Journal of Geophysical Research*, *110*, A11219. https://doi.org/10.1029/2004JA010617

Eastwood, J. P., Lucek, E. A., Mazelle, C., Meziane, K., Narita, Y., Pickett, J., & Treumann, R. (2005b). The foreshock. *Space Science Reviews*, *118*, 41–94.

Ergun, R. E., Tucker, S., Westfall, J., Goodrich, K. A., Malaspina, D. M., Summers, D., et al. (2016). The axial double probe and fields signal processing for the MMS mission. *Space Science Reviews*, *199*, 167–188. https://doi.org/10.1007/s11214-014-0115-x

Farris, M. H., Petrinec, S. M., & Russell, C. T. (1991). The thickness of the magnetosheath: Constraints on the polytropic index. *Geophysical Research Letters*, *18*(10), 1821–1824. https://doi.org/10.1029/91GL02090

Gary, S. P. (1991). Electromagnetic ion/ion instabilities and their consequences in space plasmas—A review. *Space Science Reviews*, *56*, 373–415. https://doi.org/10.1007/BF00196632

Giacalone, J., Schwartz, S. J., & Burgess, D. (1993). Observations of suprathermal ions in association with SLAMS. *Geophysical Research Letters*, *20*(2), 149–152. https://doi.org/10.1029/93GL00067

Gingell, I., Schwartz, S. J., Eastwood, J. P., Burch, J. L., Ergun, R. E., Fuselier, S., et al. (2019). Observations of magnetic reconnection in the transition region of quasi-parallel shocks. *Geophysical Research Letters*, *46*, 1177–1184. https://doi.org/10.1029/2018GL081804

Gingell, I., Schwartz, S. J., Eastwood, J. P., Stawarz, J. E., Burch, J. L., Ergun, R. E., et al. (2020). Statistics of reconnecting current sheets in the transition region of earth's bow shock. *Journal of Geophysical Research: Space Physics*, *125*, e2019JA027119. https://doi.org/10.1029/2019JA027119

Hobara, Y., Walker, S. N., Balikhin, M., Pokhotelov, O. A., Dunlop, M., Nilsson, H., & Rème, H. (2007). Characteristics of terrestrial foreshock ULF waves: Cluster observations. *Journal of Geophysical Research*, *112*, A07202. https://doi.org/10.1029/2006JA012142

Hollweg, J. V. (1994). Beat, modulational, and decay instabilities of a circularly polarized Alfvén wave. *Journal of Geophysical Research*, *99*(A12), 23431–23447. https://doi.org/10.1029/94JA02185

Hoppe, M. M., & Russell, C. T. (1983). Plasma rest frame frequencies and polarizations of the low-frequency upstream waves: ISEE 1 and 2 observations. *Journal of Geophysical Research*, *88*(A3), 2021–2027. https://doi.org/10.1029/JA088iA03p02021

Le, G., & Russell, C. T. (1994). The morphology of ULF waves in the Earth's foreshock. In M. J. Engebretson, K. Takahashi, & M. Scholer (Eds.), Solar wind sources of magnetospheric ultra-low-frequency waves, Geophysical Monograph Series (Vol. 81, pp. 87–98). Washington, DC: AGU. https://doi.org/10.1029/GM081p0087

Le, G., Russell, C. T., Thomsen, M. F., & Gosling, J. T. (1992). Observations of a new class of upstream waves with periods near 3 seconds. *Journal of Geophysical Research*, *97*(A3), 2917–2925. https://doi.org/10.1029/91JA02707

Lindqvist, P.-A., Olsson, G., Torbert, R. B., King, B., Granoff, M., Rau, D., et al. (2016). The spin-plane double probe electric field instrument for MMS. *Space Science Reviews*, *199*, 137–165. https://doi.org/10.1007/s11214-014-0116-9

Lucek, E. A., Horbury, T. S., Dandouras, I., & Rème, H. (2008). Cluster observations of the Earth's quasi-parallel bow shock. *Journal of Geophysical Research*, *113*, A07S02. https://doi.org/10.1029/2007JA012756

Mann, G., Luehr H., & Baumjohann W. (1994). Statistical analysis of short large-amplitude magnetic field structures in the vicinity of the quasi-parallel bow shock, *Journal of Geophysical Research*, *99*(A7), 13315–13323. https://doi.org/10.1029/94JA00440

Pollock, C., Moore, T., Jacques, A., Burch, J., Gliese, U., Saito, Y., et al. (2016). Fast plasma investigation for magnetospheric multiscale. *Space Science Reviews*, *199*, 331–406. https://doi.org/10.1007/s11214-016-0245-4

Robert, P., Dunlop, M. W., Roux, A., & Chanteur, G. (1998). Accuracy of current density determination. *ISSI Scientific Reports Series*, *1*, 395–418.

Russell, C. T., Anderson, B. J., Baumjohann, W., Bromund, K. R., Dearborn, D., Fischer, D., et al. (2016). The magnetospheric multiscale magnetometers. *Space Science Reviews*, *199*, 189–256. https://doi.org/10.1007/s11214-014-0057-3

Scholer, M., Kucharek, H., & Shinohara, I. (2003). Short large-amplitude magnetic structures and whistler wave precursors in a full-particle quasi-parallel shock simulation. *Journal of Geophysical Research*, *108*(A7), 1273. https://doi.org/10.1029/2002JA009820

Schwartz, S. J., & Burgess, D. (1991). Quasi-parallel shocks—A patchwork of three-dimensional structures. *Geophysical Research Letters*, *18*, 373–376. https://doi.org/10.1029/91GL00138

Schwartz, S. J., Burgess, D., Wilkinson, W. P., Kessel, R. L., Dunlop, M., & Luehr, H. (1992). Observations of short large-amplitude magnetic structures at a quasi-parallel shock. *Journal of Geophysical Research*, *97*(A4), 4209–4227. https://doi.org/10.1029/91JA02581

Thomsen, M. F., Gosling, J. T., Bame, S. J., & Russell, C. T. (1990). Magnetic pulsations at the quasi-parallel shock. *Journal of Geophysical Research*, *95*(A2), 957–966. https://doi.org/10.1029/JA095iA02p00957

Torbert, R. B., Russell, C. T., Magnes, W., Ergun, R. E., Lindqvist, P.-A., LeContel, O., et al. (2014). The FIELDS instrument suite on MMS: Scientific objectives, measurements, and data products. *Space Science Reviews*, *199*, 105–135. https://doi.org/10.1007/s11214-014-0109-8

Tsubouchi, K., & Lembège, B. (2004). Full particle simulations of short large-amplitude magnetic structures (SLAMS) in quasiparallel shocks. *Journal of Geophysical Research*, *109*, 2114. https://doi.org/10.1029/2003JA010014

Wang, S., Chen, L.-J., Bessho, N., Hesse, M., Wilson, L. B., Denton, R., et al. (2020a). Ion-scale current structures in short large-amplitude magnetic structures. *The Astrophysical Journal*, *898*, 121. https://doi.org/10.3847/1538-4357/ab9b8b

Wang, S., Chen, L.-J., Bessho, N., Hesse, M., Wilson, L. B., III, Giles, B., et al. (2019). Observational evidence of magnetic reconnection in the terrestrial bow shock transition region. *Geophysical Research Letters*, *45*, 562–570. https://doi.org/10.1029/2018GL080944

Wang, S., Chen, L.-J., Ng, J., Bessho, N., Le, G., Fung, S. F., et al. (2020b). A case study of non-resonant mode three-second ULF waves observed by MMS. *Journal of Geophysical Research: Space Physics*, *125*, e2020JA028557. https://doi.org/10.1029/2020JA028557

Weidl, M. S., Winske, D., & Niemann, C. (2019a). On the background-gyroresonant character of Bell's instability in the large-current regime. *The Astrophysical Journal*, *872*, 48. https://doi.org/10.3847/1538-4357/aafad0

Weidl, M. S., Winske, D., & Niemann, C. (2019b). Three regimes and four modes for the resonant saturation of parallel ion-beam instabilities. *The Astrophysical Journal*, *873*, 57. https://doi.org/10.3847/1538-4357/ab0462

Wilson, L. B., III (2016). Low frequency waves at and upstream of collisionless shocks. In A. Keiling, D.-H. Lee, & V. Nakariakov (Eds.), Low-frequency waves in space plasmas. Geophysical Monograph Series (Vol. 216, pp. 269–291). Washington, DC: AGU. https://doi.org/10.1002/9781119055006.ch16

Zweibel, E. G., & Everett, J. E. (2010). Environments for magnetic field amplification by cosmic rays. *The Astrophysical Journal*, *709*, 1412. https://doi.org/10.1088/0004-637X/709/2/1412